



Threshold in orbital forcing for Saharan greening lowers with rising levels of greenhouse gases

Mateo Duque-Villegas^{1,2}, Martin Claussen^{1,3}, Victor Brovkin¹, and Thomas Kleinen¹

¹Max Planck Institute for Meteorology, Hamburg, Germany

²International Max Planck Research School on Earth System Modelling, Hamburg, Germany

³Center for Earth System Research and Sustainability (CEN), Universität Hamburg, Hamburg, Germany

Correspondence: Mateo Duque-Villegas (mateo.duque@mpimet.mpg.de)

Abstract. Numerous climate archives reveal alternating arid and humid conditions in North Africa during the last several million years. Most likely the dry phases resembled current hyper-arid landscapes, whereas the wet phases known as African Humid Periods (AHPs) sustained much more surface water and greater vegetated areas that “greened” a large part of the Sahara region. Previous analyses of sediment cores from the Mediterranean Sea showed the last five AHPs differed in strength, duration and rate of change. To understand the causes of such differences we perform transient simulations of the past 190,000 years with Earth system model of intermediate complexity CLIMBER-2. We analyse amplitude and rate of change of the modelled AHPs responses to changes in orbital parameters, greenhouse gases (GHGs) and ice sheets. In agreement with estimates from Mediterranean sapropels, we find the model predicts a threshold in orbital forcing for Sahara greening and occurrence of AHPs. Maximum rates of change in simulated vegetation extent at AHP onset and termination correlate well with the rate of change of the orbital forcing. As suggested by available data for the Holocene AHP, the onset of modelled AHPs happens usually faster than termination. A factor separation analysis confirms the dominant role of the orbital forcing in driving the amplitude of precipitation and vegetation extent for past AHPs. Forcing due to changes in GHGs and ice sheets is only of secondary importance, with a small contribution from synergies with the orbital forcing. Via the factor separation we detect that the threshold in orbital forcing for AHP onset varies with GHGs levels. To explore the implication of our finding from the palaeoclimate simulations for the AHPs that might occur in a greenhouse gas-induced warmer climate, we extend the palaeoclimate simulations into the future. For the next 100,000 years the variations in orbital forcing will be smaller than during the last hundred millennia, and the insolation threshold for the onset of late Quaternary AHPs will not be crossed. However, with higher GHGs concentrations the predicted threshold drops considerably. Thereby, the occurrence of AHPs in upcoming millennia appears to crucially depend on future concentrations of GHGs.

1 Introduction

Extensive evidence from geological records indicates that the landscape across North Africa changed repeatedly back and forth from wet to dry conditions during the late Quaternary (Larrasoana et al., 2013; Grant et al., 2017). Wet phases termed African Humid Periods (AHPs) were intervals with increased rainfall, abundant lakes and rivers, as well as extended vegetation cover that “greened” large parts of the Sahara (deMenocal et al., 2000). Environmental shifts occurred at millennial timescale,



25 primarily in response to variations in the Earth's orbit, which altered the seasonal radiation budget and led to distinct regional
circulation patterns and atmospheric moisture transports (Kutzbach, 1981). This link between orbital configuration and climate
of North Africa is noticeable in proxy data (Lourens et al., 2001) and is supported by computer simulations (Tuentner et al.,
2003). Orbitally induced changes in regional circulation were amplified by several feedback processes related mainly to surface
properties such as sea temperature and land cover (Claussen et al., 2017; Pausata et al., 2020). Despite current knowledge about
30 these key mechanisms, inconsistencies between proxy data and simulations suggest there are still gaps in understanding of AHP
dynamics (Braconnot et al., 2012).

Much of what is known about AHPs stems out of the study of the last event during the Holocene epoch (Tierney et al.,
2017). The relatively vast amount of available proxy data that cover this epoch has allowed for extensive data analyses (e.g.,
Bartlein et al., 2011; Lézine et al., 2011; Shanahan et al., 2015) and numerical simulations of its AHP (e.g., Jungandreas et al.,
35 2021; Cheddadi et al., 2021; Dallmeyer et al., 2020; Chandan and Peltier, 2020). Yet the latest sediment records from the
Mediterranean Sea have highlighted the diversity in intensity of earlier AHPs (Blanchet et al., 2021; Ehrmann and Schmiedl,
2021), reaching as far back in time as Marine Isotope Stage (MIS) 6 about 190,000 years ago (190 ka). The motivation behind
this study lies in understanding the causes behind the different intensities. Although regional climate likely responded in a
similar way for all previous AHPs, paced by orbital variations described in current theory (Claussen et al., 2017), an additional
40 complication emerges from the added effects of simultaneous changes in greenhouse gases (GHGs) and the waxing and waning
of ice sheets. The two factors should act as additional forcing on the AHP response, considering that North African climate
responds to changes in both of them (Claussen et al., 2003; Marzin et al., 2013), and assuming the region in turn has a negligibly
small effect on these global climate drivers. Therefore we examine the changes in orbital, GHGs and ice sheets forcings in order
to understand how the past five AHPs differed.

45 Previous modelling studies investigated the AHP response under these forcings separately, through sensitivity experiments
that showed individually their first-order effects. For instance, Tuentner et al. (2003) described the consequences of changes
in orbital parameters, while Claussen et al. (2003) focused on GHGs and Marzin et al. (2013) on the ice sheets. However,
considering separately each forcing prevents simulation of synergical or joint effects amongst them, and therefore a direct
comparison of their individual impact on AHP response is limited. The transient experiments in Weber and Tuentner (2011),
50 Kutzbach et al. (2020) and Blanchet et al. (2021) included all three forcing factors and showed the minor role the forcing
from GHGs and ice sheets plays in setting the strength of AHPs. Nonetheless, these analyses focused more on the simulated
response of North Africa (and how it compares with proxies) than on the evolution or absolute values of the forcings. The
novelty of this work lies in our attention to the multiple forcings involved, since we look at their rates of change, threshold
values and correlations, and we present the first factor separation analyses for these forcings in North Africa. Additionally we
55 use future estimates of these forcings to simulate potential future AHP responses and assess how far our lessons from past
regional climate change can take us into the future.

Our main goal is to investigate how much each forcing mechanism, by itself and in synergy with the others, contributes to
the different AHPs intensities seen in proxy records. We use model CLIMBER-2 (Petoukhov et al., 2000; Ganopolski et al.,



2001) of intermediate complexity (Claussen et al., 2002), to study the climate response of North Africa to changes in orbital parameters, GHGs radiative forcing and extent of ice sheets. We run an ensemble of transient global climate simulations for the last 190 millennia (190 kyr) and study onset and termination dynamics of past AHPs. Using the factor separation method of Stein and Alpert (1993) we quantify individual and synergical contributions of every forcing to the magnitude of an AHP. Our findings from the past humid periods are also useful when we extend experiments for a 100 kyr into the future and assess potential consequences of changes in GHGs in relation to development of future AHPs.

65 2 Methods

2.1 Model description

CLIMBER-2 incorporates a 2.5 dimensional statistical–dynamical atmosphere model of coarse horizontal resolution of about 10° latitude and 51° longitude, and a parameterised vertical structure assuming universal profiles of temperature, humidity and meridional circulation (Petoukhov et al., 2000). The atmosphere component is coupled to a zonally averaged and multi-basin dynamic ocean model based on that of Stocker et al. (1992), with meridional resolution of 2.5° latitude and 20 vertical levels. Connected to these components the model also includes a one layer thermodynamic sea ice model with horizontal ice transport (Ganopolski and Rahmstorf, 2001), the three-dimensional polythermal ice sheet model SICOPOLIS (Greve, 1997), the dynamic global vegetation model VECODE (Brovkin et al., 1997), a dynamic global carbon cycle model with land and ocean biogeochemistry (Brovkin et al., 2002, 2007; Ganopolski and Brovkin, 2017), and modules for aeolian dust effects (Bauer and Ganopolski, 2010; Ganopolski et al., 2010).

The model has a low computational cost that enables simulations over long timescales, when multiple components of the climate system can interact. Despite its coarse spatial resolution and simplifications the model captures well past climate changes (Claussen et al., 1999a), as well as the aggregated large–scale features of modern climate (Ganopolski et al., 1998). Its response to changes in boundary conditions and climate forcings is comparable to that of more comprehensive models (Ganopolski et al., 2001), and it successfully simulates glacial–interglacial cycles (Ganopolski et al., 2010; Ganopolski and Brovkin, 2017). In fact, CLIMBER-2 is currently the only geographically explicit model which can be used for an ensemble of simulations of glacial–interglacial cycles. For the specific case of North Africa CLIMBER-2 has already been used to study its climate on multi-millennia timescales with a favourable performance (e.g., Claussen et al., 1999b, 2003; Tuenter et al., 2005; Tjallingii et al., 2008).

85 2.2 Experiments of past AHPs

We simulate the coupled atmosphere, ocean, sea ice, land surface and vegetation dynamics for the past 190 kyr. The polythermal ice sheets model and global carbon cycle model components are not employed since we prescribe ice volume and atmospheric GHGs levels using available data. Simulations start from an equilibrium state attained after a 5 kyr simulation that maintained parameters set at 190 ka values. We perform 15 transient simulations prescribing possible combinations of

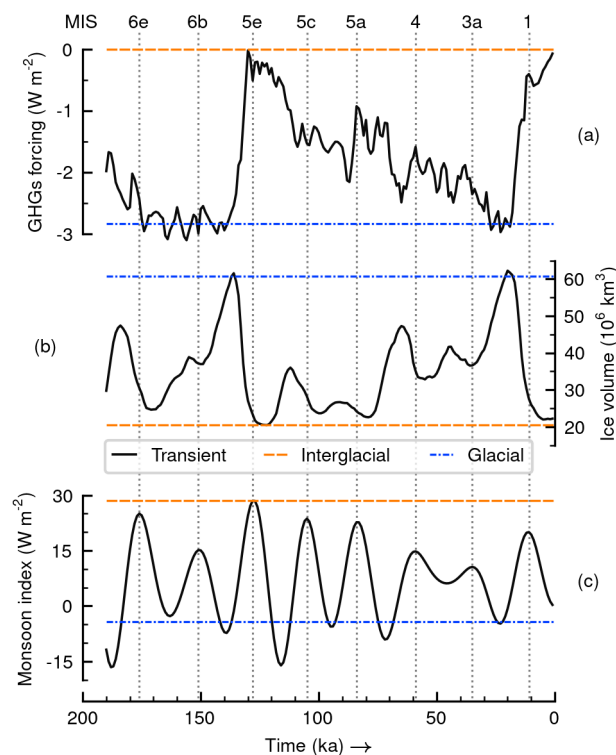


Figure 1. Prescribed forcing parameters in simulations for (a) GHGs radiative forcing, (b) ice sheets and (c) orbital forcing. Transient series come from Antarctic ice cores, modelled ice sheets data and orbital theory, respectively. Horizontal lines are cases when forcings are fixed to interglacial or glacial reference values. Vertical lines indicate maxima in the monsoon index of tropical insolation and are labelled using MIS names on top (see Appendix A about notation).

90 climate forcing factors: GHGs levels, ice sheets extent and orbital parameters. Forcings are prescribed either with a transient
series from past evidence or with a single reference value as shown in Fig. 1. Reference values are taken from the transient
series close to the Eemian interglacial state at about 125 ka and close to the Last Glacial Maximum (LGM) at about 21 ka. The
GHGs radiative forcing in Fig. 1a comes from Ganopolski and Calov (2011) and it considers variations in gases CO₂, CH₄
and N₂O that are in line with Antarctic ice cores (Petit et al., 1999; EPICA Community Members, 2004). Ice sheets data are
95 model output from a simulation also in Ganopolski and Calov (2011) which agrees with sea level changes in Waelbroeck et al.
(2002) and the reconstructions of Peltier (1994). Ice sheets are represented by a spatially distributed transient series varying
mostly in the Northern Hemisphere, albeit we show only the global cumulative ice volume (Fig. 1b). Earth's orbital parameters
(precession, obliquity and eccentricity) vary according to Berger (1978). We show their secular variations using the monsoon
index defined by Rossignol-Strick (1983), which measures an insolation gradient in the tropics relevant to monsoon systems
100 and AHPs (Fig. 1c). In the text and in Fig. 1 we label peaks in the monsoon index using MIS names to ease location of time



Table 1. Experiments and forcing settings. Entries in “Field” column indicate how a climatic variable taken from an experiment is used in the factor separation method (see Appendix B with equations). Transient series are those in Fig. 1. The future set is not part of the separation method. 0 ka is present-day and AP is after present-day.

| Name | Time | Field | Description | GHGs radiative forcing (W m^{-2}) | Ice volume (10^6 km^3) | Monsoon index (W m^{-2}) |
|------|-----------------|---|------------------------------|---|---------------------------------------|--|
| E0 | 190 ka–0 ka | f_0 | Control experiment. | Transient | Transient | Transient |
| EI1 | | $f_{I, \text{GHG}}$ | | 0.0 | Transient | Transient |
| EI2 | | $f_{I, \text{Ice}}$ | | Transient | 20.5 | Transient |
| EI3 | | $f_{I, \text{Orbital}}$ | | Transient | Transient | 28.5 |
| EI4 | 190 ka–0 ka | $f_{I, \text{GHG} + \text{Ice}}$ | Interglacial separation set. | 0.0 | 20.5 | Transient |
| EI5 | | $f_{I, \text{GHG} + \text{Orbital}}$ | | 0.0 | Transient | 28.5 |
| EI6 | | $f_{I, \text{Ice} + \text{Orbital}}$ | | Transient | 20.5 | 28.5 |
| EI7 | | $f_{I, \text{GHG} + \text{Ice} + \text{Orbital}}$ | | 0.0 | 20.5 | 28.5 |
| EG1 | | $f_{G, \text{GHG}}$ | | -2.8 | Transient | Transient |
| EG2 | | $f_{G, \text{Ice}}$ | | Transient | 60.7 | Transient |
| EG3 | | $f_{G, \text{Orbital}}$ | | Transient | Transient | -4.2 |
| EG4 | 190 ka–0 ka | $f_{G, \text{GHG} + \text{Ice}}$ | Glacial separation set. | -2.8 | 60.7 | Transient |
| EG5 | | $f_{G, \text{GHG} + \text{Orbital}}$ | | -2.8 | Transient | -4.2 |
| EG6 | | $f_{G, \text{Ice} + \text{Orbital}}$ | | Transient | 60.7 | -4.2 |
| EG7 | | $f_{G, \text{GHG} + \text{Ice} + \text{Orbital}}$ | | -2.8 | 60.7 | -4.2 |
| F0 | | – | | 0 Gt C scenario | 22.2 | Berger (1978) |
| F1 | | – | | 1000 Gt C scenario | 22.2 | Berger (1978) |
| F2 | | – | | 2000 Gt C scenario | 22.2 | Berger (1978) |
| F3 | 0 ka–100 kyr AP | – | Future set. | 3000 Gt C scenario | 22.2 | Berger (1978) |
| F4 | | – | | 4000 Gt C scenario | 22.2 | Berger (1978) |
| F5 | | – | | 5000 Gt C scenario | 22.2 | Berger (1978) |

slices when AHPs usually occur. Details about forcings, computation of the monsoon index and MIS nomenclature are given in Appendix A.

Experiments of past AHPs and their forcing setup combinations follow the factor separation method of Stein and Alpert (1993) for three factors: (1) GHGs radiative forcing, (2) ice sheets extent and (3) orbital parameters. Using this method it is possible to estimate individual and synergical contributions of the forcing factors to a simulation outcome (or predicted climatic field). We are interested in knowing how much the forcings contribute to the simulation of AHPs. To implement the method a specific simulation target must be chosen in order to calculate deviations from the baseline or control state (i.e., the



factor separation depends on the target or point of view). We choose two simulation targets with opposing global climates and AHP situations: the Eemian interglacial around 125 ka (i.e., warm global climate) with a strong AHP and the LGM around 110 21 ka (i.e., cold global climate) with no AHP. Experiments and forcings combinations are shown in Table 1. Only in the control experiment E0 all forcings vary realistically as in the transient series obtained from past data (see Fig. 1). For the rest of experiments we have two sets of simulations using the interglacial or glacial reference values shown in Table 1, with all possible “fixed-or-transient” combinations in each set. For instance, simulation EI4 has both GHGs forcing and ice sheets fixed at the interglacial reference values for the entire 190 kyr run (i.e., they are kept constant at interglacial levels). Likewise for 115 EG4 but instead the fixed values are the glacial levels. Experiments EI7 and EG7 have the three forcings fixed at their respective reference points. Details and equations of the separation analyses are given in Appendix B.

2.3 Experiments of future AHPs

The low computational cost of the model and information available about future changes in the forcings enable us to also look into potential future climate change in North Africa. We are interested in knowing how much our findings from the past can 120 inform the future. Additional simulations start from present-day conditions in the control experiment E0 and cover the next 100 millennia after present (kyr AP). Projections of GHGs radiative forcing are based on the CO₂ emissions scenarios of Archer and Brovkin (2008), which differ by the cumulative amount of carbon released to the atmosphere in units of gigatonnes of carbon (Gt C). Five experiments include a scenario of null emissions since preindustrial conditions (0 Gt C), a “moderate” emissions scenario with a release of 1000 Gt C, a “large” emissions scenario with a release of 5000 Gt C, and the intermediate 125 cases of 2000, 3000 and 4000 Gt C. In these scenarios 90 % of the emissions are assumed to occur within the first few centuries of simulation, meaning there is an early peak of atmospheric concentration of CO₂ that subsequently decays to an equilibrium value (higher than preindustrial). These experiments are also shown in Table 1. For these simulations we ignore the radiative forcing effect of other GHGs. The orbital forcing is considered to continue changing following Berger (1978). We keep the ice sheets fixed at the preindustrial setting, neglecting the effects of a potential complete deglaciation or a new glacial inception. 130 The latter is justified since a large ice sheet should not emerge within the next 100 kyr AP, even for the moderate emissions scenario (Ganopolski et al., 2016).

3 Results

We study model output of century-mean values of near-surface air temperature, daily precipitation and fractional vegetation coverage in the Sahara region. In the model the Sahara is located in one grid box spanning approximately 20–30° N and 15° W– 135 50° E. Temperature and precipitation are resolved daily in the model, hence we include seasonal averages for them, whereas vegetation is resolved annually, thus only annual mean values are reported. Summer refers to the June–July–August average, while winter to the December–January–February average.

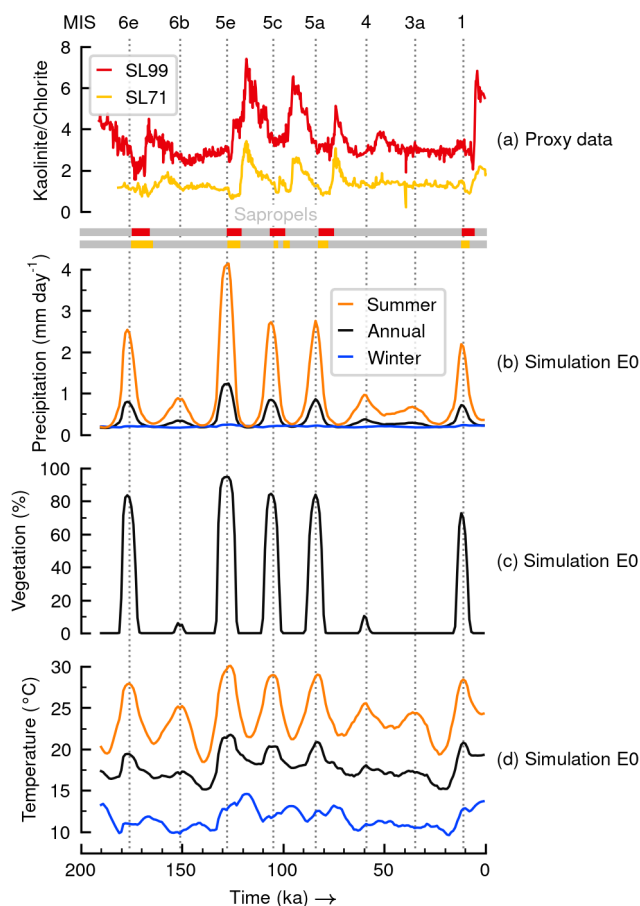


Figure 2. Comparison of (a) proxy data with modelling results in Sahara for (b) daily precipitation, (c) vegetation fraction and (d) near-surface temperature in control simulation E0. Proxy data are clay minerals ratios and sapropel layers from two sediment cores from Eastern Mediterranean described in Ehrmann and Schmiedl (2021). Vertical lines indicate maxima in the monsoon index of tropical insolation and are labelled using MIS names on top.

3.1 Simulation of past AHPs

Results of the control simulation E0 are shown in Fig. 2 alongside proxy data from sediment cores from the Eastern Mediterranean Sea (Ehrmann and Schmiedl, 2021). The proxies in Fig. 2a show dust pulses of clay minerals found always following a sapropel layer in the sediments. Sapropel layers indicate past instances of AHPs, while the amplitudes of the dust pulses are linked to the strength of the hydrological cycle during their preceding AHPs. The comparison between the proxy data and our simulations can only be qualitative in nature, since we do not model either dust transport into the Mediterranean Sea nor sapropel formation. It is remarkable, however, that the control simulation E0 (Fig. 2b–d) shows large peaks close in time with the sapropel layers in the proxies. Also both in simulation E0 and the proxies the strongest signals happen during MIS 5e.



Table 2. Results in Sahara of annual mean values in control experiment E0 taken near maxima of the monsoon index of tropical insolation. Sapropel layers are those in Fig. 2a. Values in parentheses are winter and summer means.

| MIS | Time (ka) | Forcing values | | | Simulated responses | | | |
|-----|-----------|---------------------------------------|---------------------------------------|--|---------------------------------------|---|-------------------|----------------|
| | | GHGs forcing (W m^{-2}) | Ice volume (10^6 km^3) | Monsoon index (W m^{-2}) | Temperature ($^{\circ}\text{C}$) | Precipitation (mm day^{-1}) | Vegetation (%) | Sapropel layer |
| 6e | 176 | -2.4 | 30.5 | 25.0 | 19.4 (11.0, 27.9) | 0.8 (0.2, 2.5) | 83.5 | Yes |
| 6b | 151 | -3.0 | 37.1 | 15.1 | 17.3 (10.1, 25.2) | 0.3 (0.2, 0.9) | 6.1 | No |
| 5e | 128 | -0.5 | 23.3 | 28.5 | 21.6 (13.0, 30.0) | 1.2 (0.2, 4.1) | 94.5 | Yes |
| 5c | 105 | -1.5 | 28.2 | 23.6 | 20.3 (12.0, 29.0) | 0.8 (0.2, 2.7) | 84.4 | Yes |
| 5a | 84 | -0.9 | 24.1 | 22.7 | 20.8 (12.5, 29.0) | 0.9 (0.2, 2.8) | 83.8 | Yes |
| 4 | 59 | -1.6 | 35.1 | 14.8 | 18.0 (10.9, 25.6) | 0.4 (0.2, 1.0) | 10.4 | No |
| 3a | 35 | -2.4 | 36.6 | 10.5 | 17.3 (10.6, 24.4) | 0.3 (0.2, 0.7) | 0.0 | No |
| 1 | 11 | -0.4 | 27.5 | 20.0 | 20.8 (12.8, 28.4) | 0.7 (0.2, 2.2) | 72.6 | Yes |

The simulation E0 is in closer agreement with the data from core SL71, where the pulses after MIS 5c and 5a have similar magnitude.

Simulation E0 shows peak values of precipitation, vegetation fraction and temperature in the Sahara region coincide with peaks in the monsoon index during the past 190 kyr. The peak values are summarised in Table 2. In the case of precipitation (Fig. 2b) and temperature (Fig. 2d) this is most conspicuous in the summer seasonal means, with large peaks similarly as evident as those in the vegetation fraction (Fig. 2c). The strongest peak values occur during the last two interglacial periods at stages MIS 5e and 1, as well as during stages MIS 6e, 5c and 5a. Only these five MIS periods have a vegetation fraction above 70 %. The vegetation peaks happen during warmer periods when annual mean daily precipitation is greater than 0.7 mm day^{-1} . This can accumulate to more than 250 mm year^{-1} , well above the minimum limit estimated to support perennial grasslands and savanna biome types in North Africa (Larrasoana et al., 2013). Although this precipitation value is low compared to estimates from proxy data (Braconnot et al., 2012), any amount over 200 mm year^{-1} is still distinctly greater than present-day values across the region (Bartlein et al., 2011), and is within the variability range of more sophisticated climate models for the last AHP during the Holocene (Harrison et al., 2015). Therefore we consider these peak times to be simulated past AHPs with CLIMBER-2. The oldest one at MIS 6e was also found by Tuenter et al. (2005), and those at MIS 5c, 5a and 1, agree with the results of Tjallingii et al. (2008). Measuring from the moment the modelled vegetation starts growing until the moment it vanishes (Fig. 2c), the AHPs last on average 10.8 kyr, with the one at MIS 5e being the longest (12 kyr) and the one at MIS 1 the shortest (9 kyr).

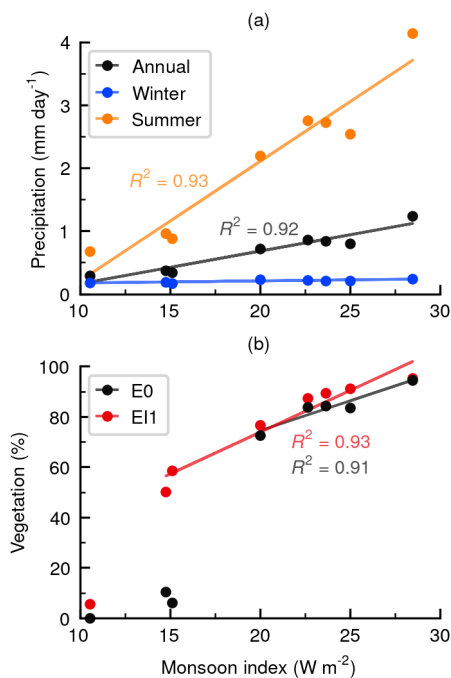


Figure 3. Correlation of orbital forcing with modelled responses in Sahara in control simulation E0 for mean values of (a) daily precipitation and (b) vegetation fraction. In (b) we also include the modelled vegetation from experiment EI1 with fixed interglacial GHGs.

3.2 Correlation of forcings and AHPs

A first approximation to study the effects of the forcings on the modelled AHP response uses a simple linear regression analysis. With the values from Table 2 we plot paired combinations of forcings and response variables in phase diagrams and fit regression lines with the ordinary least-squares method and use the statistic R^2 and the p -value of the F-statistic as goodness-of-fit estimates. The forcings are included in the regression analysis (besides the modelled response) because even though we know that GHGs levels and ice sheets are not independent from the orbital forcing, we do not know exactly how they relate to each other during AHPs. We also reckon GHGs and ice sheets are global features while the monsoon index is a regional insolation gradient. We find there is a strong correlation ($R^2 = 0.75$, p -value = 0.006) between the average ice sheets volume and the monsoon index, with the highest monsoon index values having the least ice volume. In contrast, we see a weak correlation ($R^2 = 0.27$, p -value = 0.19) between the GHGs radiative forcing and the tropical insolation gradient imposed by the orbital forcing.

The modelled response correlates strongly with the monsoon index as shown in Fig. 3. For precipitation (Fig. 3a) we observe a positive linear relationship for summer seasonal ($R^2 = 0.93$, p -value = 0.0001) and annual ($R^2 = 0.92$, p -value = 0.0001) means, therefore higher monsoon index values yield higher precipitation in the Sahara region. Winter precipitation being almost a flat line shows this modelled variable in Sahara does not depend on the monsoon index. In the case of vegetation (Fig. 3b)

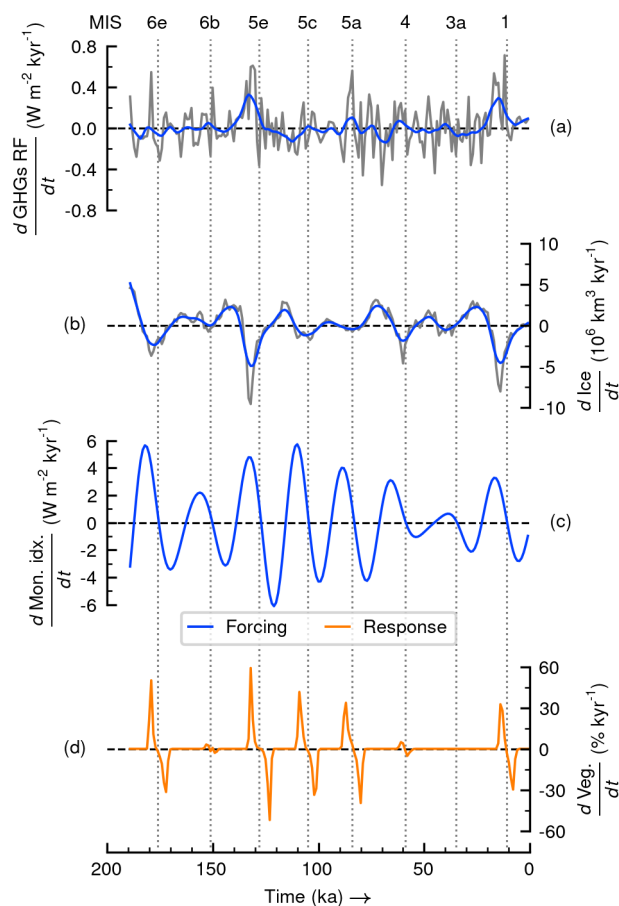


Figure 4. Rates of change of forcings and modelled vegetation in control experiment E0: (a) GHGs Radiative Forcing (RF), (b) global ice volume, (c) monsoon index and (d) vegetation fraction in Sahara. GHGs and ice volume series are smoothed using a Locally Weighted Scatterplot Smoothing (LOWESS) filter of 15 kyr. Vertical lines show maxima of monsoon index of tropical insolation and are labelled using MIS names on top.

we see non-linear behaviour with an abrupt large jump from low (about 10 %) to high (about 70 %) vegetation coverage within a small range of variation of the monsoon index from around 15 to 20 W m^{-2} . Only for vegetation a signal change-point analysis yields one clear change-point at 20 W m^{-2} (not shown; Killick et al., 2012). Vegetation values occurring past the threshold range have a strong correlation ($R^2 = 0.91$, p -value = 0.012) with the monsoon index. We also include in Fig. 3b the vegetation response of sensitivity simulation EI1 (with interglacial GHGs forcing) because it shows that the insolation threshold might be sensitive to the GHGs forcing. With interglacial GHGs radiative forcing (experiment EI1) the threshold decreases below 15 W m^{-2} and the correlation past this threshold between vegetation and monsoon index is still strong ($R^2 = 0.93$, p -value = 0.0005).



Table 3. Rates of change of forcings and modelled vegetation in control simulation E0 at times of peak rates in vegetation response. Only shown are MIS stages with an AHP response. For GHGs Radiative Forcing (RF) and global ice volume the values are from the smoothed series in Fig. 4.

| MIS | Time (ka) | Forcings | | | Response |
|------------------------|-----------|---|--|---|--|
| | | $\frac{d\text{GHGs RF}}{dt}$ ($\text{W m}^{-2} \text{kyr}^{-1}$) | $\frac{d\text{Ice}}{dt}$ ($10^6 \text{ km}^3 \text{ kyr}^{-1}$) | $\frac{d\text{Mon. idx.}}{dt}$ ($\text{W m}^{-2} \text{kyr}^{-1}$) | $\frac{d\text{Veg.}}{dt}$ ($\% \text{ kyr}^{-1}$) |
| <i>Inception AHP</i> | | | | | |
| 6e | 179 | 0.0 | -2.3 | 4.2 | 50.1 |
| 5e | 132 | 0.3 | -4.9 | 4.8 | 59.2 |
| 5c | 109 | -0.1 | -0.8 | 5.4 | 41.6 |
| 5a | 87 | 0.1 | -0.3 | 3.6 | 33.7 |
| 1 | 14 | 0.3 | -4.6 | 2.5 | 32.6 |
| <i>Termination AHP</i> | | | | | |
| 6e | 172 | 0.0 | -0.8 | -3.0 | -31.6 |
| 5e | 123 | 0.0 | -0.1 | -5.3 | -52.1 |
| 5c | 102 | 0.0 | -0.8 | -3.2 | -33.7 |
| 5a | 80 | 0.0 | -0.1 | -3.1 | -39.7 |
| 1 | 8 | 0.0 | -1.2 | -2.1 | -29.8 |

3.3 Speed of change of AHPs

Proxy data indicates that past AHPs were different not only in magnitude, but also in their rates of change (Ehrmann et al., 2017). Figure 4 shows finite differences with respect to time in the forcings and modelled vegetation response in the control experiment E0. The radiative forcing from the GHGs increases quickly towards positive values just before the two interglacial states at MIS 5e and 1 (Fig. 4a). Everywhere else GHGs changes happen relatively slowly and erratically. Ice volume changes happen more smoothly. There is a strong and quick reduction of ice sheets before interglacial states at MIS 5e and 1 (Fig. 4b). Then milder in strength follow the ice reduction speeds just before stages MIS 6e, 5c and 4. During MIS 5a the ice sheets do not change as much prior to the monsoon index peak, however, soon after it there is a relatively quick growth of ice sheets. For the monsoon index we notice that extreme speeds of growth and decline occur around the vertical lines (Fig. 4c), where the maximum values happen (inflection points). The fastest increases in monsoon index occur at stages MIS 6e and 5c. Then follow closely stages at MIS 5e and 5a. Remaining stages have relatively weaker speeds of change for this variable. The fastest reduction in the monsoon index happens after stage MIS 5e.

Figure 4 shows that the changes in the vegetation response do not follow linearly one single forcing. Nevertheless, they share the inflection points with the monsoon index rate of change, having both maximum growth and decline speeds around

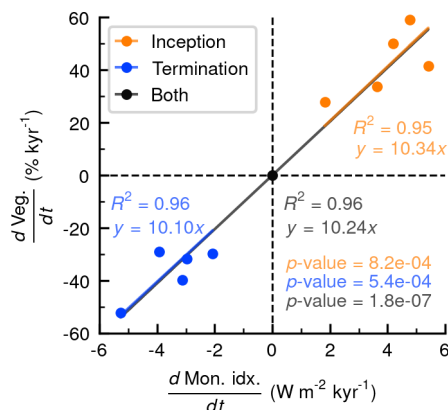


Figure 5. Correlation of peak rates of change in vegetation response in Sahara versus rates of change in monsoon index during AHP inception and termination in control simulation E0.

200 the vertical lines. Vegetation growth maxima occur always about 2.0 kyr after the monsoon index peak rates of change, while maximum vegetation decline rate occurs on average 2.4 kyr before the minimum peaks in monsoon index speed of change (Fig. 4d). Peak rates of positive and negative change are summarised in Table 3. The fastest vegetation growth rates occur at stages MIS 6e and 5e, while the slowest happens at MIS 1. The fastest decline rates in vegetation are seen after MIS 5e and 5a. In general, we see that the maximum vegetation growth speeds are faster than subsequent declining rates, the clearest example
 205 being MIS 6e. Only at MIS 5a the opposite is true.

Table 3 shows that the strongest vegetation growth rate during the AHP inception in MIS 5e occurs simultaneously with the strongest increase rate in GHGs radiative forcing and the strongest reduction rate in ice volume, in spite of the monsoon index increase rate not being the largest. Most likely during AHP inception in MIS 1, the increasing rate of GHGs radiative forcing and the strong reduction of ice sheets compensated for the slow rate of change in monsoon index. In the case of terminations
 210 of AHPs, the leading factor contributing to the speed of vegetation decline is the change in the monsoon index. Figure 5 shows the relationship between these two rates of change during inception and termination of AHPs. We find a strong correlation ($R^2 = 0.96$, $p\text{-value} < 0.0001$) between the speed of change in the monsoon index and the peak speed of growth and decline of vegetation in the model. The larger the positive (negative) monsoon index change rate, the larger the growth (decline) rate in vegetation during AHP inception (termination). The residual errors in the regression lines presumably include the effects of
 215 the changes in the other forcings.

3.4 Factor separation analyses

We suspect that differences in intensity amongst AHPs should be mainly determined by differences in the state of GHGs, ice sheets and orbital configuration at the time they occur. However, we do not know how much each of the forcings is affecting the AHPs intensities. To look into this we perform simulations according to the factor separation method of Stein and Alpert



220 (1993) and implement its equations (see Appendix B) using the model output for annual means of temperature, precipitation and vegetation fraction in the Sahara region. Because the separation method depends on the chosen simulation target we carry out two analyses: one of them isolates the contributions of the forcing factors to attain an Eemian-like strong AHP response (i.e., interglacial perspective), while another one does it for an LGM-like non-AHP response (i.e., glacial perspective).

Both target responses for the two separation analyses are represented in simulations EI7 and EG7. Simulation EI7 from the interglacial perspective has all three forcing factors fixed at interglacial conditions (using the Eemian as reference). In this simulation modelled Saharan temperature stays for all times at 21.8 °C, precipitation at 1.3 mm day⁻¹ and vegetation fraction at 95.8 %. These values resemble those around the Eemian peak (about 125 ka) in the control simulation E0 (see Fig. 2). Simulation EG7 from the glacial perspective has forcings fixed at glacial conditions (using LGM as reference). In this simulation modelled Saharan temperature remains for all times at 15.2 °C, precipitation at 0.2 mm day⁻¹ and vegetation fraction at 0.0 %. These values resemble those around the LGM (about 21 ka) in the control simulation E0 (see Fig. 2). Therefore, the interglacial perspective experiment EI7 keeps a permanent strong Eemian-like AHP for the entire simulation, whereas the glacial EG7 keeps none. Through the factor separation method we then estimate how much each of the forcings is contributing at all times to the differences between the control experiment E0 and targets EI7 (strong AHP) and EG7 (no AHP).

235 Results of the separation analysis from the interglacial perspective are shown in Fig. 6 for AHP temperature, precipitation and vegetation fraction. With the forcing factors fixed at interglacial levels the modelled response in EI7 (Eemian-like AHP) deviates always positively from the control experiment E0 for the three climatic variables. This is as expected since the resulting values of EI7 in the previous paragraph are higher than those in the control E0 at all times (only Eemian in E0 is close to EI7). The relevant outcome of the separation method is in the colours in Fig. 6, which show how the forcings contribute to the EI7 – E0 difference. For AHP temperature (Fig. 6a) the individual contribution of each forcing is directly proportional to the change in the forcing. To see this it is necessary to compare differences between the control forcing values in the transient series in Fig. 1 and the interglacial reference level in that same figure. For instance, at stage MIS 6b the largest contribution to temperature change comes from the GHGs radiative forcing change (Fig. 6a), since that is the forcing with the largest difference between the transient series and the interglacial horizontal line (see Fig. 1a). For the AHP temperature response the synergistic effects are small in comparison to the individual contributions. Averaging the contributions to AHP temperature for the whole time series in Fig. 6a yields that GHGs add about 1.6 °C (41.1 % of change from E0), ice sheets 0.8 °C (19.9 % of change from E0) and the orbital forcing 1.8 °C (45.9 % of change from E0). The synergy between GHGs and the orbital forcing is the one with the largest effect adding in average about –0.2 °C (–4.9 % of change from E0).

250 The AHP precipitation case in the separation analysis is different to the temperature one. Figure 6b shows that the AHP precipitation response largely depends on the orbital forcing. Not only the individual contribution of this forcing is the largest for all times, but also its synergies with the other two forcings have relatively large effects. The individual contribution of the GHGs radiative forcing to changes in AHP precipitation is small. The individual effects of ice sheets on AHP precipitation are negligible as well. No synergistic effects exist between the ice sheets forcing and the GHGs radiative forcing. Averaging

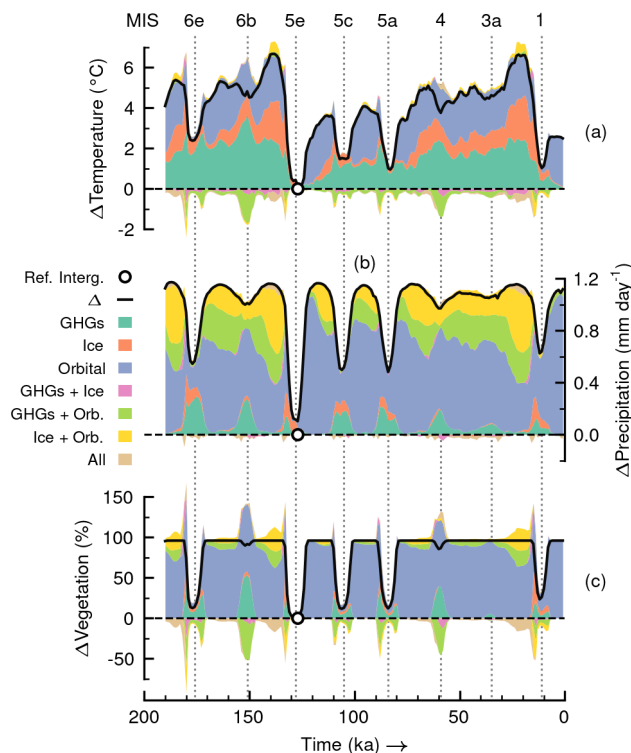


Figure 6. Factor separation analysis in Sahara from interglacial perspective for annual means of (a) near-surface temperature, (b) daily precipitation and (c) vegetation fraction. Colours indicate contributions from individual forcings and related synergies to the total deviation in EI7 (Eemian-like AHP) from the control experiment ($\Delta = EI7 - E0$). A marker shows the location of the reference interglacial state, where the difference between EI7 and E0 is minimum. Vertical lines indicate maxima of monsoon index of tropical insolation and are labelled using MIS names on top.

the contributions to AHP precipitation for the whole time series in Fig. 6b we obtain that GHGs add about 0.1 mm day^{-1} (6.7 % of change from E0), ice sheets close to 0.0 mm day^{-1} (2.2 % of change from E0) and the orbital forcing about 0.6 mm day^{-1} (59.3 % of change from E0). Both synergies of the orbital forcing with GHGs and ice sheets round up each one to 0.2 mm day^{-1} (each about 15 % of change from E0). This means the effects of the orbital forcing and these two synergies with GHGs and ice sheets amount to about 90.9 % of the change from E0.

AHP vegetation results in Fig. 6c are similar to the AHP precipitation case, although the individual effect of the orbital forcing is much more conspicuous (predominant blue colour). The negative synergistic effects seen in the vegetation changes are an artefact of the separation analysis method because vegetation is a bounded quantity. Consider, for example, the time around 150 ka during MIS 6b, when the Sahara is much greener, close to a 100 % vegetation cover, in simulation EI7 than in simulation E0 (Fig. 6c). The individual contribution of orbital forcing (blue colour) would make some 90 % of the Sahara green, and the GHGs forcing (muted green colour) some 50 %. If both forcings are active, then the pure contributions do not



265 add linearly, because the Sahara cannot be more than 100 % covered with vegetation. Therefore, the synergy between these forcings (light green colour) has to be negative. Average contributions to AHP vegetation for the whole series in Fig. 6c are about 5.8 % from GHGs (6.4 % of change from E0), 2.2 % from ice sheets (2.4 % of change from E0) and 72.6 % from the orbital forcing (79.5 % of change from E0). The synergy (when positive) between GHGs and orbital forcing adds in average about 4.0 % (4.4 % of change from E0) while the synergy (when positive) between ice sheets and orbital forcing about 5.3 %
270 (5.8 % of change from E0). The orbital forcing and all of its synergies account for about 90.4 % of vegetation change from E0.

From the glacial perspective in the additional separation analysis we obtain qualitatively similar results (Fig. C1). In this case the deviations in EG7 from the control E0 are always negative for the three climatic variables and the effects of the ice sheets changes are larger than those of the GHGs. Nonetheless, the same behaviour for temperature is observed, with changes being proportional to the changes in the forcings. We also see the orbital forcing as the main contributor to the reductions in
275 precipitation and vegetation that keep the non-AHP conditions during glacial times. From this perspective synergies are more difficult to assess because of the lower bounds in precipitation (0 mm day^{-1}) and vegetation (0 %). Details of this separation analysis are given in Appendix C.

3.5 AHPs in scenarios of future climate change

When computing the monsoon index for the next 100 kyr AP (millennia after present) we see that the onset threshold of past
280 AHPs (between $15\text{--}20 \text{ W m}^{-2}$ in the model) will not be crossed within the next some 60 kyr (Fig. 7a). The amplitude in the monsoon index (proxy for orbital forcing) is much smaller than that of past times (see Fig. 1) due to low eccentricity in the Earth's orbit. Only for the time around 66 kyr AP the monsoon index approaches the onset threshold. From the sensitivity simulation EI1 in which the GHGs forcing is set to interglacial level, we already find the orbital threshold can change (see Fig. 3b). Hence we expect that in a climate with much stronger GHGs forcing (Fig. 7b) the threshold might decrease even
285 further. The simulations F0–5 corroborate the lesson learnt from the study of the past (see Fig. 7c). Emissions scenarios in the simulations have a peak GHGs forcing at the start since they assume that 90 % of carbon is released within the first centuries. As mentioned in Section 2.3, we assume that global ice volume stays close to its current low level and ignore the effects of a total deglaciation or a new glacial inception.

The modelled vegetation response in Fig. 7c shows the potential effects of increased GHGs radiative forcing for climate
290 in the Sahara. The no-emissions scenario (0 Gt C) predicts that no AHP should occur before the next 60 kyr AP. For this scenario only at 66 kyr AP (named peak M4) the threshold of the monsoon index of tropical insolation is approached slightly at 16.5 W m^{-2} , and we see a vegetation response of about 54.1 %. However, for the “moderate” emissions scenario (1000 Gt C) we see already that additional vegetation responses begin to occur at earlier monsoon index peaks. These mild responses at other monsoon index peaks are amplified as the GHGs radiative forcings increase with the scenarios. For the “large” emissions
295 scenario (5000 Gt C) the response at 9 kyr AP (named peak M1) with monsoon index of only 9.2 W m^{-2} is already at about 89.9 %, which is higher than that of the strongest monsoon index peak M4 for any scenario. Therefore we see that the effect of the large GHGs radiative forcing in the early 60 kyr AP of simulation is compensating for the low monsoon index values

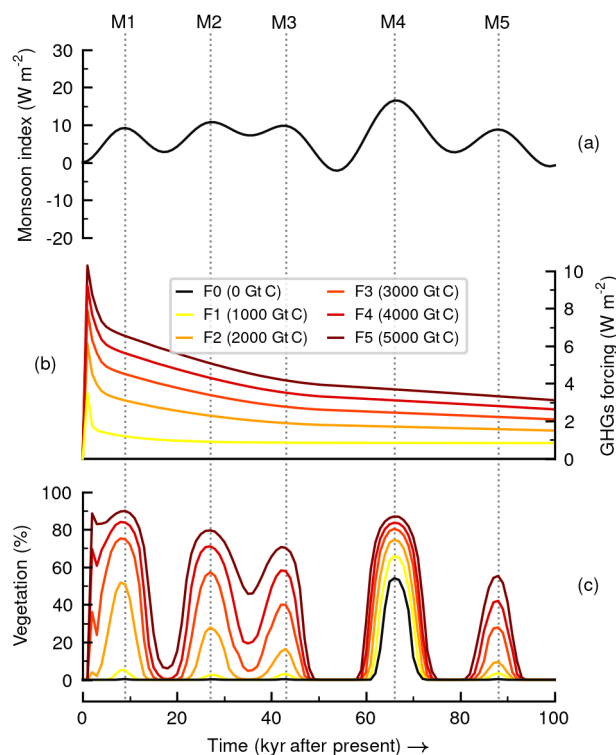


Figure 7. AHPs in future climate change scenarios for the next 100 kyr AP: (a) computed monsoon index changes, (b) scenarios of GHGs radiative forcing and (c) modelled vegetation fraction in Sahara. Vertical lines indicate future peaks in monsoon index of tropical insolation. Total cumulative emissions of carbon are shown in parentheses in the legend.

during this time. Nonetheless, this effect is only seen at the monsoon index peaks, therefore the orbital forcing is still the triggering mechanism for the AHP response.

300 4 Discussion

We initially assess the ability of model CLIMBER-2 to simulate past occurrences of AHPs during glacial–interglacial cycles. Our results agree with previous efforts which also found the model’s performance adequate (e.g., Tuenter et al., 2005; Tjallingii et al., 2008). Magnitude and timing of the simulated AHPs compare favourably not only with the proxy data in Ehrmann and Schmiedl (2021), but also with the data and simulations of Blanchet et al. (2021) and Kutzbach et al. (2020). Although
305 comparison between simulations is limited due to large differences in spatial resolution, one difference that might be discussed is the magnitude of the simulated Holocene AHP. In the case of Blanchet et al. (2021) the AHP during the Holocene is stronger than those at MIS 5c and 5a. Our simulations show the opposite, in agreement with the simulations in Kutzbach et al. (2020). To reconcile this we can look at the sediment records from the Mediterranean Sea discussed in Ehrmann and Schmiedl (2021) and



say that simulations of Saharan climate in CLIMBER-2 evolve like the proxy data from semi-distal sites off the North African
310 coastline, whereas those in Blanchet et al. (2021) resemble the data from proximal sites. Spatial heterogeneity of the changes
during AHPs hinders model consistency with all proxy data. Nevertheless our simulations show a reasonable representation of
the evolution of the climate in the Sahara during the last 190 kyr and this enables us to study the effects of forcing from GHGs,
ice sheets and orbital parameters.

Analysis of our control simulation reveals that the AHP response in CLIMBER-2 is highly correlated with the variations of
315 the monsoon index (proxy for orbital forcing based on a gradient in tropical insolation). This correlation was also found in the
data of Rossignol-Strick (1983) and Ehrmann et al. (2017). We find that there is a critical value of the monsoon index that must
be crossed to simulate Saharan greenings with the model. Past this threshold vegetation and precipitation feed back through
biogeophysical changes and the climatic response in Sahara is amplified resulting in an AHP (Brovkin et al., 1998; Claussen
et al., 1999b). Such non-linear responses from monsoon regions are also seen in proxy data (Rossignol-Strick, 1983; Ziegler
320 et al., 2010). The threshold value lies somewhere between 15 and 20 $W m^{-2}$. Depending on the strength of additional factors
(such as GHGs or ice sheets) the threshold could be closer to the lower or the upper boundary of this range. Below 15 $W m^{-2}$
until about 10 $W m^{-2}$ the model simulates only a weak vegetation response that cannot develop into an AHP, probably because
within this range the amplifying feedback between vegetation and precipitation is not yet effective. Rossignol-Strick (1983)
found that the threshold for occurrence of sapropel layers in sediment cores from the Mediterranean Sea (an indication of past
325 AHPs) is about 19.8 $W m^{-2}$ (41 Langley day⁻¹). How close this value is from the estimate from CLIMBER-2 is useful as
additional validation for the model, even though we simulate Saharan greening and not sapropel formation.

From the control simulation we also find that the speed at which the AHP response occurs correlates well with the speed
of change in the monsoon index. This is valid during AHP onset and termination. However for the fastest growth rate of
vegetation to occur, it is important that the trends of change in the ice sheets and the GHGs radiative forcing are also favourable.
330 For instance, at AHP onset during MIS 5e the three forcing factors are synchronised with increasing monsoon index, strong
reduction of ice sheets and an increasing rate of warming from GHGs radiative forcing. Another example occurs at onset during
the Holocene AHP, when a modest increasing rate in the monsoon index is compensated by simultaneous negative trend in ice
sheets and warming trend from GHGs. Synchronisation of the forcings can explain why the speed of the modelled AHP onset
is generally faster than the subsequent AHP termination. This was also described for the Holocene AHP by Shanahan et al.
335 (2015). Because of a lag in the ice sheets rate of change with respect to the monsoon index change, and because of the erratic
rate of change in the GHGs, the three forcing factors are not usually in sync during AHPs terminations and the rate of change is
generally slower than their onset. The only AHP termination that is faster than its onset occurs in stage MIS 5a, when a strong
increase in ice sheets happens closely after the monsoon index negative peak rate of change. In Lézine et al. (2011) the role
of groundwater is described to explain why there is a rapid response during AHP onset and a subsequent slower more gradual
340 AHP termination (with aquifers providing base flow). However, the model's hydrology does not include this feature and we
focus only on the speeds of the forcings and their synchronisation.



We complement the study of the control simulation with a factor separation analysis. Its outcome confirms the dominant role of the orbital forcing in setting the amplitude of the modelled precipitation and vegetation responses of past AHPs. This was already described, for instance, in Tuentler et al. (2003), Kutzbach et al. (2020) and Blanchet et al. (2021). In particular, a factor analysis in Blanchet et al. (2021) showed that the individual roles of the GHGs radiative forcing and the global ice volume are of secondary importance for the strength of simulated AHPs. What we do with the factor separation method is quantitative estimates of said dominance or secondary importance of these forcings. From our results, when we add together the individual contributions from GHGs and ice sheets to the AHP precipitation or vegetation coverage responses, we find they amount to less than 20 % of the change induced by the orbital forcing alone. In fact, according to the simulations the orbital forcing alone (without effects from GHGs and ice sheets) should account for about 60 % (80 %) of changes in the AHP precipitation (vegetation) during the last 190 kyr. If its synergies are included, then the orbital forcing is responsible for more than 90 % of precipitation and vegetation changes. The factor separation also shows that GHGs and ice sheets have a larger impact on precipitation (and vegetation extent) when in synergy with the orbital forcing than individually. For near-surface temperature, in contrast, all the three forcing factors have a large effect individually and the synergies are all small in comparison.

After analysing the influence of the forcing factors on past AHP responses, we then evaluate the potential for future occurrences of humid periods. During the next 100 kyr AP the effects of changes in GHGs radiative forcing become larger while those of the orbital forcing become weaker. The future of the ice sheets is more uncertain, but a glacial inception is not likely to happen (Ganopolski et al., 2016) and if we ignore potential catastrophic consequences of a complete deglaciation, the impact of the ice sheets on AHPs should not change much from its current interglacial-like effect. Claussen et al. (2003) and D'Agostino et al. (2019) already studied AHPs under future climate change and showed how a dynamically orbitally driven AHP response differs from a thermodynamically GHGs-driven AHP. Therefore we do not focus on the mechanisms that explain such differences but on the relative importance of each forcing during the AHP response. The main finding is that the GHGs radiative forcing has an amplification effect on the simulated vegetation response that is large enough to overcome the limiting threshold for Sahara greening imposed by the orbital forcing. An alternative interpretation is that the GHGs forcing lowers the tropical insolation requirement for AHP onset. Here it is important to mention that we are neglecting biogeochemical effects, since we prescribe GHGs levels, therefore potential effects of feedbacks between the carbon cycle and vegetation are being ignored. The AHP responses are still paced by precession variations but the increased atmospheric moisture (product of GHGs radiative warming) compensates for a weaker gradient in insolation.

5 Conclusions

We have used the climate model of intermediate complexity CLIMBER-2 to assess the role on AHP strength of three climate forcing factors: Earth's orbital parameters, GHGs radiative forcing and ice sheets extent. Consistent with previous studies we find the model simulates reasonably well the evolution of past AHPs in terms of timing and magnitude. A newly discovered feature is the model contains the threshold behaviour of AHPs associated with the orbital forcing previously found in proxy data. For the Saharan greening response during AHPs, the simulated threshold in the monsoon index of tropical insolation lies



375 within 15 and 20 W m^{-2} . Besides this critical value, the monsoon index (proxy of orbital forcing) also correlates well with the simulated precipitation and vegetation responses during AHPs, not only with their magnitudes, but also with their rates of change: higher monsoon index values lead to higher magnitudes and faster changes. We show also that for fast changes to occur it is important that the forcings are synchronised. In the simulations this happens most often during AHP onset than termination and therefore the onset rate of change is generally faster.

380 In addition to the results from a control experiment we include two complete factor separation analyses that make explicit the dominant role of the orbital forcing setting the strength of past AHPs. The individual effects of the GHGs and ice sheets put together cause less than 20 % of the change induced by the orbital forcing. The effects of GHGs and ice sheets are notably greater when in synergy with the orbital forcing than separately. When we add together the effects of the orbital forcing and its synergies it amounts to over 90 % of the change in the AHP precipitation and vegetation responses. Despite the dominance
385 of the orbital forcing, when we extend the simulations to cover the next 100 kyr AP we find that increased GHGs radiative forcing lowers the critical value of monsoon index that must be crossed to simulate Saharan greening and the subsequent AHP response.

These findings both support previous research and contribute new insights to our understanding of AHPs dynamics. In several cases we are able to extrapolate previous knowledge from the Holocene AHP to earlier humid periods. In general the
390 results agree with the consensus on predominance of the orbital forcing and make explicit the minor role that additional forcing from GHGs and ice sheets played during previous AHPs. However, because we consider both past and future simulations of AHPs we are able to show that GHGs may be more important than previously thought. A key message from this work is that even though the orbital forcing is the leading factor setting intensity and timing of AHPs, the atmospheric levels of GHGs have the potential to lower the insolation requirement for AHP onset. Such an effect of GHGs in the past might have been hidden
395 by the strength of the non-linear response to the orbital forcing, combined with a relatively narrow range of GHGs variability, yet it may be particularly important when considering future occurrences of AHPs under climate change scenarios.

Code and data availability. Model source code of CLIMBER-2 is available upon request. Data and post-processing Python scripts to reproduce the authors' work are archived by the Max Planck Institute for Meteorology and are accessible without any restrictions at <http://hdl.handle.net/21.11116/0000-000A-1217-8>. The Ehrmann and Schmedl (2021) data in Fig. 2 are available at <https://doi.org/10.1594/PANGAEA.923491>, last access: 13 May 2021. The Lisiecki and Raymo (2005) data shown in Fig. A1 are available at <http://lorraine-lisiecki.com/LR04stack.txt>, last access: 16 December 2020.
400

Appendix A: Forcings, monsoon index and MIS notation

Experiments with CLIMBER-2 differ only in the input data concerning the GHGs radiative forcing, the extent of ice sheets and orbital parameters (precession, obliquity and eccentricity). The GHGs radiative forcing input series agrees with data from
405 Antarctic ice cores (Petit et al., 1999; EPICA Community Members, 2004). It is described in Ganopolski et al. (2010) as an



Table A1. Orbital parameters in CLIMBER-2 simulations.

| Forcing type | Precession (longitude of perihelion) | Obliquity | Eccentricity | Monsoon index |
|-------------------|--------------------------------------|---------------|---------------|---------------|
| Transient | Berger (1978) | Berger (1978) | Berger (1978) | Berger (1978) |
| Interglacial-like | 261.271° | 24.124° | 0.039 | 28.5 |
| Glacial-like | 97.771° | 22.787° | 0.019 | -4.2 |

equivalent CO₂ concentration (C_e) that includes variations of CO₂, CH₄ and N₂O. The total GHGs radiative forcing (ΔRF) is computed as

$$\Delta RF = 5.35 \ln \frac{C_e}{C_0}, \quad (\text{A1})$$

where C_0 is set to 280 ppm. The reference values for glacial and interglacial conditions are about 165 ppm and 280 ppm of equivalent CO₂ respectively, which translate using Eq. A1 into the radiative forcing values summarised in Table 1.

In the case of ice sheets, Fig. 1 shows only a global cumulative sum. For our simulations the input for the model is a gridded time series that is itself model output from an earlier simulation by Ganopolski and Calov (2011), who ran CLIMBER-2 model employing the ice sheets model component SICOPOLIS (Greve, 1997). The ice sheets evolution is in agreement with the sea level changes data from Waelbroeck et al. (2002) and the ice sheets maps of Peltier (1994). The reference values in this case are actually maps taken from the gridded series during the Eemian around 124 ka and the LGM around 21 ka. Their global cumulative ice volumes are those seen in Table 1. Sea level change corresponding to the Eemian ice sheets map is -0.21 m, while that of the LGM is -106.44 m.

CLIMBER-2 by default computes the orbital parameters using the formulae of Berger (1978). In the experiments with fixed orbital forcing, we switch off the module for the Berger (1978) computation, and fix the values of precession (i.e., angle from autumnal equinox to perihelion), obliquity and eccentricity to those calculated for the Eemian and LGM periods. These values are shown in Table A1. To summarise them into a single value we use the monsoon index defined by Rossignol-Strick (1983). To compute the index it is necessary first to compute the cumulative insolation during the northern caloric summer season defined by Milankovitch (1941). We do this using the daily insolation values computed with the Berger (1978) theory and the equations presented in Vernekar (1972). The caloric summer insolation is obtained for latitudes at the North Tropic near 23.45° N (I_T) and at the Equator (I_E) and then the monsoon index (MI) at millennia before the present-day time slice t is

$$MI^t = 2I_T^t - I_E^t. \quad (\text{A2})$$

Figure 1 shows in fact the variations in the monsoon index from the 1950 Common Era (CE) reference value of about 482 W m⁻² (around 995 Langley day⁻¹). Because AHPs occur usually at peak times of this index, it is convenient for the discussion to be able to identify every monsoon index maximum. Therefore, to label them we use the MIS stage (or substage) name that occurred at the time of the monsoon index maximum. This is also useful because MIS names give hints about the

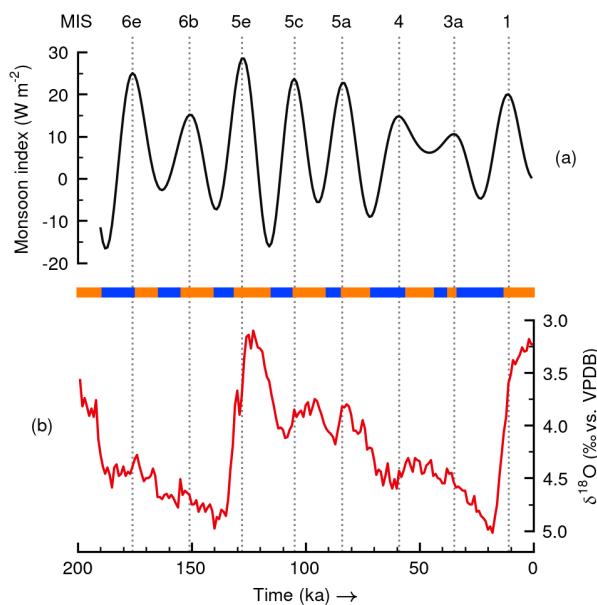


Figure A1. Notation for peaks of (a) monsoon index uses MIS labels on top, following the scheme in Railsback et al. (2015), who used the (b) Lisiecki and Raymo (2005) marine isotope stack data to label the time slices shown in a bar with different colours. The isotope data are with respect to the standard Vienna Peedee Belemnite (VPDB). Vertical lines indicate the monsoon index peaks.

state of the climate system at the time. In spite of there not being consensus in some of the names, here we make use of the notation scheme put forth by Railsback et al. (2015). Figure A1 shows the monsoon index in the control experiment and the Lisiecki and Raymo (2005) dataset used by Railsback et al. (2015). In Fig. A1 a thin bar with coloured boxes shows the different periods they identified. Vertical lines then help us choosing the names for each monsoon index peak.

435 **Appendix B: Equations of separation analyses**

We perform experiments following the separation method of Stein and Alpert (1993). In this case it is done for three factors: (1) GHGs radiative forcing, (2) global ice volume and (3) orbital parameters. Consequently 2^3 simulations are needed for one separation analysis. The technique uses deviations of a simulation target with respect to a baseline or control state (experiment E0). We choose two different simulation targets: (1) global interglacial conditions with a strong AHP, and (2) global glacial conditions with no AHPs. The targets correspond to simulations EI7 and EG7 respectively. Therefore we do two separation analysis for AHPs: one from an interglacial perspective and another from a glacial one. The equations for the separation

440

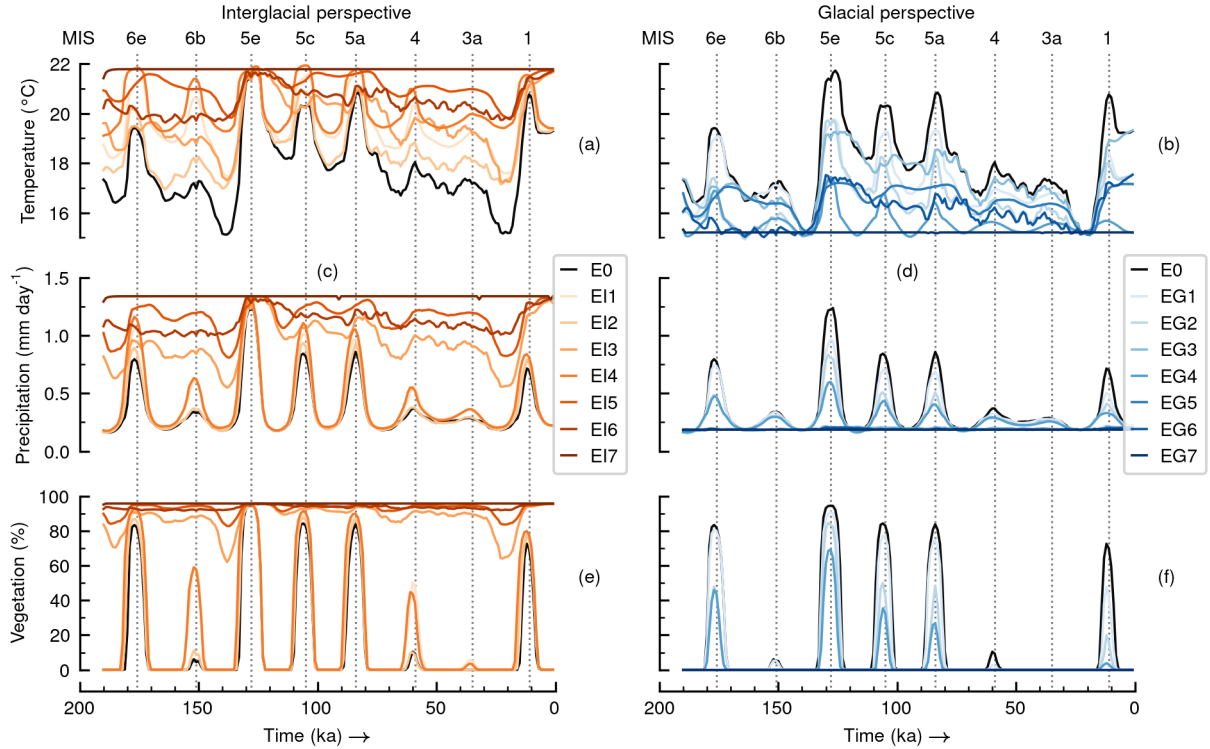


Figure A2. Results of annual means of (a, b) near-surface temperature, (c, d) daily precipitation and (e, f) vegetation fraction in the Sahara for all simulations involved in the separation analyses from interglacial and glacial perspectives. Vertical lines indicate monsoon index maxima and are labelled using MIS names on top.

analysis from the interglacial perspective are

$$\hat{f}_0 = f_0, \quad (\text{B1})$$

$$\hat{f}_{I, \text{GHG}} = f_{I, \text{GHG}} - f_0, \quad (\text{B2})$$

$$445 \quad \hat{f}_{I, \text{Ice}} = f_{I, \text{Ice}} - f_0, \quad (\text{B3})$$

$$\hat{f}_{I, \text{Orbital}} = f_{I, \text{Orbital}} - f_0, \quad (\text{B4})$$

$$\hat{f}_{I, \text{GHG} + \text{Ice}} = f_{I, \text{GHG} + \text{Ice}} - (f_{I, \text{GHG}} + f_{I, \text{Ice}}) + f_0, \quad (\text{B5})$$

$$\hat{f}_{I, \text{GHG} + \text{Orbital}} = f_{I, \text{GHG} + \text{Orbital}} - (f_{I, \text{GHG}} + f_{I, \text{Orbital}}) + f_0, \quad (\text{B6})$$

$$\hat{f}_{I, \text{Ice} + \text{Orbital}} = f_{I, \text{Ice} + \text{Orbital}} - (f_{I, \text{Ice}} + f_{I, \text{Orbital}}) + f_0, \quad (\text{B7})$$

$$450 \quad \hat{f}_{I, \text{GHG} + \text{Ice} + \text{Orbital}} = f_{I, \text{GHG} + \text{Ice} + \text{Orbital}} - (f_{I, \text{GHG} + \text{Ice}} + f_{I, \text{GHG} + \text{Orbital}} + f_{I, \text{Ice} + \text{Orbital}}) + (f_{I, \text{GHG}} + f_{I, \text{Ice}} + f_{I, \text{Orbital}}) - f_0, \quad (\text{B8})$$

where letters with hats in the left-hand side are the estimated effects on the simulation outcome of each forcing factor alone when having a single subscript or together in synergy with others when multiple subscripts. The letters on the right-hand side



(known as climatic fields) represent the model output for a variable taken from the set of experiments part of the analysis. Therefore what is shown in Fig. 2 are the fields f_0 from simulation E0 for temperature, precipitation and vegetation. Likewise
 455 $f_{I, GHG + Ice + Orbital}$ represents the variables when taken from simulation EI7. All fields for these variables are shown in Fig. A2, including all the other simulations. For the separation analysis from the glacial perspective the equations are

$$\hat{f}_0 = f_0, \quad (B9)$$

$$\hat{f}_{G, GHG} = f_{G, GHG} - f_0, \quad (B10)$$

$$\hat{f}_{G, Ice} = f_{G, Ice} - f_0, \quad (B11)$$

$$460 \hat{f}_{G, Orbital} = f_{G, Orbital} - f_0, \quad (B12)$$

$$\hat{f}_{G, GHG + Ice} = f_{G, GHG + Ice} - (f_{G, GHG} + f_{G, Ice}) + f_0, \quad (B13)$$

$$\hat{f}_{G, GHG + Orbital} = f_{G, GHG + Orbital} - (f_{G, GHG} + f_{G, Orbital}) + f_0, \quad (B14)$$

$$\hat{f}_{G, Ice + Orbital} = f_{G, Ice + Orbital} - (f_{G, Ice} + f_{G, Orbital}) + f_0, \quad (B15)$$

$$\hat{f}_{G, GHG + Ice + Orbital} = f_{G, GHG + Ice + Orbital} - (f_{G, GHG + Ice} + f_{G, GHG + Orbital} + f_{G, Ice + Orbital}) + (f_{G, GHG} + f_{G, Ice} + f_{G, Orbital}) - f_0, \quad (B16)$$

465 where now, for instance, there is $f_{G, GHG + Ice + Orbital}$ to represent the variables taken from simulation EG7. We do a total of 15 simulations (and not 16) for the two separation analyses because they share the same baseline state E0.

Appendix C: Glacial separation analysis

The factor separation analysis from the glacial perspective is shown in Fig. C1. In this case deviations in EG7 from the control experiment E0 are negative. In simulation EG7 there is a permanent non-AHP state. Different to the interglacial case, the effect
 470 of the ice sheets is larger than that of the GHGs or the orbital forcing in some cases. Saharan temperature negative changes in Fig. C1a happen everywhere except during glaciations before the Eemian interglacial around 140 ka and the LGM. Average contributions to temperature change during the series at times close to peaks of monsoon index in Fig. C1a (when changes are most visible) are $-1.0\text{ }^\circ\text{C}$ from GHGs (-25.8% of change from E0), $-2.0\text{ }^\circ\text{C}$ (-49.4% of change from E0) from ice sheets and $-1.5\text{ }^\circ\text{C}$ from orbital forcing (-38.6% of change from E0). There is a rather small counteracting (positive) temperature
 475 change from the synergy between ice sheets and orbital forcing that amounts to about $0.5\text{ }^\circ\text{C}$ ($+13.1\%$ of change from E0).

Glacial precipitation (Fig. C1b) and vegetation (Fig. C1c) reductions only occur at peak times of the monsoon index (where AHPs occur in control E0). For these two variables the deviations from the control experiment are bounded at 0 mm day^{-1} and 0% . Due to these bounds the synergies are not reliable and they show in Fig. C1 as the symmetrical opposite shapes of their individual contributions for GHGs and ice sheets. Average contributions to precipitation reductions near monsoon index peaks
 480 in Fig. C1b (not the whole series) are about -0.1 mm day^{-1} from GHGs (-13.0% of change from E0), -0.2 mm day^{-1} from ice sheets (-27.0% of change from E0) and -0.4 mm day^{-1} from orbital forcing (-54.0% of change from E0). For vegetation change near times of peak monsoon index in Fig. C1c (not the whole series) contributions average about -7.3% from GHGs

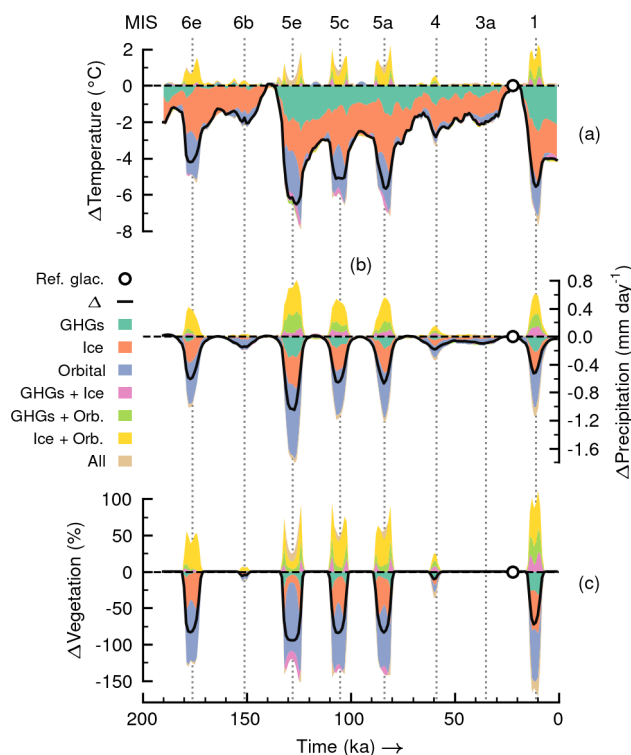


Figure C1. Factor separation analysis in Sahara from glacial perspective for annual means of (a) near-surface temperature, (b) daily precipitation and (c) vegetation fraction. Colours indicate contributions from individual forcings and related synergies to the total deviation in EG7 (glacial non-AHP) from the control experiment ($\Delta = EG7 - E0$). A marker shows the location of the reference glacial state, where the difference between EG7 and E0 is minimum. Vertical lines indicate monsoon index maxima and are labelled using MIS names on top.

(−8.3 % of change from E0), −26.0 % from ice sheets (−29.0 % of change from E0) and −49.0 % from orbital forcing (55.0 % of change from E0). We reach a similar conclusion as from the interglacial perspective: contributions to temperature are proportional to the size of the change in the forcings, while for precipitation and temperature the orbital forcing changes are the main cause of change.

Author contributions. MC, VB and MDV designed the research idea. TK and VB contributed to the experimental design and provided model code and input data. MDV performed the model experiments. All authors contributed to the analysis of results and to the preparation of the manuscript.

490 *Competing interests.* At least one of the (co-)authors is a member of the editorial board of *Climate of the Past*. The peer-review process was guided by an independent editor and the authors have no other competing interests to declare.



495 *Acknowledgements.* We thank Roberta D’Agostino (MPI-M) for helpful comments on an earlier version of the manuscript. Gerhard Schmiedl (UHH), Jürgen Böhner (UHH) and Jürgen Bader (MPI-M) provided valuable input and discussions. Jochem Marotzke (MPI-M), Dallas Murphy and participants of “S_41 Advanced Scientific Writing” (2021) also helped improve the writing in the manuscript. This work contributes to the project “African and Asian Monsoon Margins” of the Cluster of Excellence EXC 2037: Climate, Climatic Change, and Society (CLICCS). We acknowledge support of the German Climate Computing Center (DKRZ) in providing computing resources and assistance. The article processing charges for this publication were covered by the Max Planck Society. Data analysis and figures were produced using Python, including libraries NumPy, Matplotlib, xarray, SciPy, pandas, statsmodels, seaborn, sdt-python and cftime.



References

- 500 Archer, D. and Brovkin, V.: The millennial atmospheric lifetime of anthropogenic CO₂, *Climatic Change*, 90, 283–297, <https://doi.org/10.1007/s10584-008-9413-1>, 2008.
- Bartlein, P. J., Harrison, S. P., Brewer, S., Connor, S., Davis, B. A. S., Gajewski, K., Guiot, J., Harrison-Prentice, T. I., Henderson, A., Peyron, O., Prentice, I. C., Scholze, M., Seppä, H., Shuman, B., Sugita, S., Thompson, R. S., Viau, A. E., Williams, J., and Wu, H.: Pollen-based continental climate reconstructions at 6 and 21 ka: a global synthesis, *Climate Dynamics*, 37, 775–802, <https://doi.org/10.1007/s00382-010-0904-1>, 2011.
- 505 Bauer, E. and Ganopolski, A.: Aeolian dust modeling over the past four glacial cycles with CLIMBER-2, *Global and Planetary Change*, 74, 49–60, <https://doi.org/10.1016/j.gloplacha.2010.07.009>, 2010.
- Berger, A.: Long-term variations of daily insolation and Quaternary climatic changes, *Journal of the Atmospheric Sciences*, 35, 2362–2367, [https://doi.org/10.1175/1520-0469\(1978\)035<2362:LTVODI>2.0.CO;2](https://doi.org/10.1175/1520-0469(1978)035<2362:LTVODI>2.0.CO;2), 1978.
- 510 Blanchet, C. L., Osborne, A. H., Tjallingii, R., Ehrmann, W., Friedrich, T., Timmermann, A., Brückmann, W., and Frank, M.: Drivers of river reactivation in North Africa during the last glacial cycle, *Nature Geoscience*, pp. 1–7, <https://doi.org/10.1038/s41561-020-00671-3>, 2021.
- Braconnot, P., Harrison, S. P., Kageyama, M., Bartlein, P. J., Masson-Delmotte, V., Abe-Ouchi, A., Otto-Bliesner, B., and Zhao, Y.: Evaluation of climate models using palaeoclimatic data, *Nature Climate Change*, 2, 417–424, <https://doi.org/10.1038/nclimate1456>, 2012.
- Brovkin, V., Ganopolski, A., and Svirezhev, Y.: A continuous climate-vegetation classification for use in climate-biosphere studies, *Ecological Modelling*, 101, 251–261, [https://doi.org/10.1016/S0304-3800\(97\)00049-5](https://doi.org/10.1016/S0304-3800(97)00049-5), 1997.
- 515 Brovkin, V., Claussen, M., Petoukhov, V., and Ganopolski, A.: On the stability of the atmosphere-vegetation system in the Sahara/Sahel region, *Journal of Geophysical Research: Atmospheres*, 103, 31 613–31 624, <https://doi.org/10.1029/1998JD200006>, 1998.
- Brovkin, V., Bendtsen, J., Claussen, M., Ganopolski, A., Kubatzki, C., Petoukhov, V., and Andreev, A.: Carbon cycle, vegetation, and climate dynamics in the Holocene: Experiments with the CLIMBER-2 model, *Global Biogeochemical Cycles*, 16, 86–1, <https://doi.org/10.1029/2001GB001662>, 2002.
- 520 Brovkin, V., Ganopolski, A., Archer, D., and Rahmstorf, S.: Lowering of glacial atmospheric CO₂ in response to changes in oceanic circulation and marine biogeochemistry, *Paleoceanography*, 22, PA4202, <https://doi.org/10.1029/2006PA001380>, 2007.
- Chandan, D. and Peltier, W. R.: African humid period precipitation sustained by robust vegetation, soil, and lake feedbacks, *Geophysical Research Letters*, 47, e2020GL088 728, <https://doi.org/10.1029/2020GL088728>, 2020.
- 525 Cheddadi, R., Carré, M., Nourelbait, M., François, L., Rhoujjati, A., Manay, R., Ochoa, D., and Schefuß, E.: Early Holocene greening of the Sahara requires Mediterranean winter rainfall, *Proceedings of the National Academy of Sciences*, 118, <https://doi.org/10.1073/pnas.2024898118>, 2021.
- Claussen, M., Brovkin, V., Ganopolski, A., Kubatzki, C., Petoukhov, V., and Rahmstorf, S.: A new model for climate system analysis: Outline of the model and application to palaeoclimate simulations, *Environmental Modeling & Assessment*, 4, 209–216, <https://doi.org/10.1023/A:1019016418068>, 1999a.
- 530 Claussen, M., Kubatzki, C., Brovkin, V., Ganopolski, A., Hoelzmann, P., and Pachur, H. J.: Simulation of an abrupt change in Saharan vegetation in the mid-Holocene, *Geophysical research letters*, 26, 2037–2040, <https://doi.org/10.1029/1999GL900494>, 1999b.
- Claussen, M., Mysak, L., Weaver, A., Crucifix, M., Fichetef, T., Loutre, M.-F., Weber, S., Alcamo, J., Alexeev, V., Berger, A., Calov, R., Ganopolski, A., Goosse, H., Lohmann, G., Lunkeit, F., Mokhov, I., Petoukhov, V., Stone, P., and Wang, Z.: Earth system



- 535 models of intermediate complexity: closing the gap in the spectrum of climate system models, *Climate Dynamics*, 18, 579–586, <https://doi.org/10.1007/s00382-001-0200-1>, 2002.
- Claussen, M., Brovkin, V., Ganopolski, A., Kubatzki, C., and Petoukhov, V.: Climate change in northern Africa: The past is not the future, *Climatic Change*, 57, 99–118, <https://doi.org/10.1023/A:1022115604225>, 2003.
- Claussen, M., Dallmeyer, A., and Bader, J.: Theory and modeling of the African Humid Period and the green Sahara, in: Oxford Research
540 Encyclopedia of Climate Science, pp. 1–39, Oxford University Press, <https://doi.org/10.1093/acrefore/9780190228620.013.532>, 2017.
- Dallmeyer, A., Claussen, M., Lorenz, S. J., and Shanahan, T.: The end of the African Humid Period as seen by a transient comprehensive Earth system model simulation of the last 8000 years, *Climate of the Past*, 16, 117–140, <https://doi.org/10.5194/cp-16-117-2020>, 2020.
- deMenocal, P. B., Ortiz, J., Guilderson, T., Adkins, J., Sarnthein, M., Baker, L., and Yarusinsky, M.: Abrupt onset and termination of the African Humid Period: rapid climate responses to gradual insolation forcing, *Quaternary Science Reviews*, 19, 347–361,
545 [https://doi.org/10.1016/S0277-3791\(99\)00081-5](https://doi.org/10.1016/S0277-3791(99)00081-5), 2000.
- D’Agostino, R., Bader, J., Bordoni, S., Ferreira, D., and Jungclaus, J.: Northern Hemisphere monsoon response to mid-Holocene orbital forcing and greenhouse gas-induced global warming, *Geophysical Research Letters*, 46, 1591–1601, <https://doi.org/10.1029/2018GL081589>, 2019.
- Ehrmann, W. and Schmiedl, G.: Nature and dynamics of North African humid and dry periods during the last 200,000 years
550 documented in the clay fraction of eastern mediterranean deep-sea sediments, *Quaternary Science Reviews*, 260, 106 925, <https://doi.org/10.1016/j.quascirev.2021.106925>, 2021.
- Ehrmann, W., Schmiedl, G., Beuscher, S., and Krüger, S.: Intensity of African humid periods estimated from Saharan dust fluxes, *PloS One*, 12, <https://doi.org/10.1371/journal.pone.0170989>, 2017.
- EPICA Community Members: Eight glacial cycles from an Antarctic ice core, *Nature*, 429, 623–628, <https://doi.org/10.1038/nature02599>,
555 2004.
- Ganopolski, A. and Brovkin, V.: Simulation of climate, ice sheets and CO₂ evolution during the last four glacial cycles with an Earth system model of intermediate complexity, *Climate of the Past*, 13, 1695–1716, <https://doi.org/10.5194/cp-13-1695-2017>, 2017.
- Ganopolski, A. and Calov, R.: The role of orbital forcing, carbon dioxide and regolith in 100 kyr glacial cycles, *Climate of the Past*, 7, 1415–1425, <https://doi.org/10.5194/cp-7-1415-2011>, 2011.
- 560 Ganopolski, A. and Rahmstorf, S.: Rapid changes of glacial climate simulated in a coupled climate model, *Nature*, 409, 153–158, <https://doi.org/10.1038/35051500>, 2001.
- Ganopolski, A., Rahmstorf, S., Petoukhov, V., and Claussen, M.: Simulation of modern and glacial climates with a coupled global model of intermediate complexity, *Nature*, 391, 351–356, <https://doi.org/10.1038/34839>, 1998.
- Ganopolski, A., Petoukhov, V., Rahmstorf, S., Brovkin, V., Claussen, M., Eliseev, A., and Kubatzki, C.: CLIMBER-2: a climate system
565 model of intermediate complexity. Part II: model sensitivity, *Climate Dynamics*, 17, 735–751, <https://doi.org/10.1007/s003820000144>, 2001.
- Ganopolski, A., Calov, R., and Claussen, M.: Simulation of the last glacial cycle with a coupled climate ice-sheet model of intermediate complexity, *Climate of the Past*, 6, 229–244, <https://doi.org/10.5194/cp-6-229-2010>, 2010.
- Ganopolski, A., Winkelmann, R., and Schellnhuber, H. J.: Critical insolation–CO₂ relation for diagnosing past and future glacial inception,
570 *Nature*, 529, 200–203, <https://doi.org/10.1038/nature16494>, 2016.



- Grant, K. M., Rohling, E. J., Westerhold, T., Zabel, M., Heslop, D., Konijnendijk, T., and Lourens, L.: A 3 million year index for North African humidity/aridity and the implication of potential pan-African Humid periods, *Quaternary Science Reviews*, 171, 100–118, <https://doi.org/10.1016/j.quascirev.2017.07.005>, 2017.
- Greve, R.: A continuum–mechanical formulation for shallow polythermal ice sheets, *Philosophical Transactions of the Royal Society of London. Series A: Mathematical, Physical and Engineering Sciences*, 355, 921–974, <https://doi.org/10.1098/rsta.1997.0050>, 1997.
- 575 Harrison, S. P., Bartlein, P. J., Izumi, K., Li, G., Annan, J., Hargreaves, J., Braconnot, P., and Kageyama, M.: Evaluation of CMIP5 palaeo-simulations to improve climate projections, *Nature Climate Change*, 5, 735–743, <https://doi.org/10.1038/nclimate2649>, 2015.
- Jungandreas, L., Hohenegger, C., and Claussen, M.: Influence of the representation of convection on the mid-Holocene West African Monsoon, *Climate of the Past*, 17, 1665–1684, <https://doi.org/10.5194/cp-17-1665-2021>, 2021.
- 580 Killick, R., Fearnhead, P., and Eckley, I. A.: Optimal detection of changepoints with a linear computational cost, *Journal of the American Statistical Association*, 107, 1590–1598, <https://doi.org/10.1080/01621459.2012.737745>, 2012.
- Kutzbach, J. E.: Monsoon climate of the early Holocene: climate experiment with the earth’s orbital parameters for 9000 years ago, *Science*, 214, 59–61, <https://doi.org/10.1126/science.214.4516.59>, 1981.
- Kutzbach, J. E., Guan, J., He, F., Cohen, A. S., Orland, I. J., and Chen, G.: African climate response to orbital and glacial forcing in 140,000-y simulation with implications for early modern human environments, *Proceedings of the National Academy of Sciences*, 117, 2255–2264, <https://doi.org/10.1073/pnas.1917673117>, 2020.
- 585 Larrasoaña, J. C., Roberts, A. P., and Rohling, E. J.: Dynamics of green Sahara periods and their role in hominin evolution, *PloS ONE*, 8, e76514, <https://doi.org/10.1371/journal.pone.0076514>, 2013.
- Lézine, A.-M., Hély, C., Grenier, C., Braconnot, P., and Krinner, G.: Sahara and Sahel vulnerability to climate changes, lessons from Holocene hydrological data, *Quaternary Science Reviews*, 30, 3001–3012, <https://doi.org/10.1016/j.quascirev.2011.07.006>, 2011.
- Lisiecki, L. E. and Raymo, M. E.: A Pliocene-Pleistocene stack of 57 globally distributed benthic $\delta^{18}\text{O}$ records, *Paleoceanography*, 20, <https://doi.org/10.1029/2004PA001071>, 2005.
- Lourens, L. J., Wehausen, R., and Brumsack, H. J.: Geological constraints on tidal dissipation and dynamical ellipticity of the Earth over the past three million years, *Nature*, 409, 1029–1033, <https://doi.org/10.1038/35059062>, 2001.
- 595 Marzin, C., Braconnot, P., and Kageyama, M.: Relative impacts of insolation changes, meltwater fluxes and ice sheets on African and Asian monsoons during the Holocene, *Climate Dynamics*, 41, 2267–2286, <https://doi.org/10.1007/s00382-013-1948-9>, 2013.
- Milankovitch, M.: *Kanon der Erdbestrahlung und seine Anwendung auf das Eiszeitenproblem*, vol. 83, Königlich Serbische Akademie, Belgrad, 1941.
- Pausata, F. S. R., Gaetani, M., Messori, G., Berg, A., de Souza, D. M., Sage, R. F., and deMenocal, P. B.: The Greening of the Sahara: Past Changes and Future Implications, *One Earth*, 2, 235–250, <https://doi.org/10.1016/j.oneear.2020.03.002>, 2020.
- 600 Peltier, W. R.: Ice age paleotopography, *Science*, 265, 195–201, <https://doi.org/10.1126/science.265.5169.195>, 1994.
- Petit, J. R., Jouzel, J., Raynaud, D., Barkov, N. I., Barnola, J. M., Basile, I., Bender, M., Chappellaz, J., Davis, M., Delaygue, G., et al.: Climate and atmospheric history of the past 420000 years from the Vostok ice core, Antarctica, *Nature*, 399, 429, <https://doi.org/10.1038/20859>, 1999.
- 605 Petoukhov, V., Ganopolski, A., Brovkin, V., Claussen, M., Eliseev, A., Kubatzki, C., and Rahmstorf, S.: CLIMBER-2: a climate system model of intermediate complexity. Part I: model description and performance for present climate, *Climate Dynamics*, 16, 1–17, <https://doi.org/10.1007/PL00007919>, 2000.



- 610 Railsback, L. B., Gibbard, P. L., Head, M. J., Voarintsoa, N. R. G., and Toucanne, S.: An optimized scheme of lettered marine isotope substages for the last 1.0 million years, and the climatostratigraphic nature of isotope stages and substages, *Quaternary Science Reviews*, 111, 94–106, <https://doi.org/10.1016/j.quascirev.2015.01.012>, 2015.
- Rossignol-Strick, M.: African monsoons, an immediate climate response to orbital insolation, *Nature*, 304, 46–49, <https://doi.org/10.1038/304046a0>, 1983.
- Shanahan, T. M., McKay, N. P., Hughen, K. A., Overpeck, J. T., Otto-Bliesner, B., Heil, C. W., King, J., Scholz, C. A., and Peck, J.: The time-transgressive termination of the African Humid Period, *Nature Geoscience*, 8, 140–144, <https://doi.org/10.1038/ngeo2329>, 2015.
- 615 Stein, U. and Alpert, P.: Factor separation in numerical simulations, *Journal of the Atmospheric Sciences*, 50, 2107–2115, [https://doi.org/10.1175/1520-0469\(1993\)050<2107:FSINS>2.0.CO;2](https://doi.org/10.1175/1520-0469(1993)050<2107:FSINS>2.0.CO;2), 1993.
- Stocker, T. F., Wright, D. G., and Mysak, L. A.: A zonally averaged, coupled ocean-atmosphere model for paleoclimate studies, *Journal of Climate*, 5, 773–797, <https://www.jstor.org/stable/26197126>, 1992.
- Tierney, J. E., Pausata, F. S. R., and deMenocal, P. B.: Rainfall regimes of the Green Sahara, *Science Advances*, 3, e1601503, <https://doi.org/10.1126/sciadv.1601503>, 2017.
- 620 Tjallingii, R., Claussen, M., Stuut, J.-B. W., Fohlmeister, J., Jahn, A., Bickert, T., Lamy, F., and Röhl, U.: Coherent high-and low-latitude control of the northwest African hydrological balance, *Nature Geoscience*, 1, 670–675, <https://doi.org/10.1038/ngeo289>, 2008.
- Tuenter, E., Weber, S. L., Hilgen, F. J., and Lourens, L. J.: The response of the African summer monsoon to remote and local forcing due to precession and obliquity, *Global and Planetary Change*, 36, 219–235, [https://doi.org/10.1016/S0921-8181\(02\)00196-0](https://doi.org/10.1016/S0921-8181(02)00196-0), 2003.
- 625 Tuenter, E., Weber, S. L., Hilgen, F. J., Lourens, L. J., and Ganopolski, A.: Simulation of climate phase lags in response to precession and obliquity forcing and the role of vegetation, *Climate Dynamics*, 24, 279–295, <https://doi.org/10.1007/s00382-004-0490-1>, 2005.
- Vernekar, A. D.: Long-period global variations of incoming solar radiation, in: *Long-Period Global Variations of Incoming Solar Radiation*, vol. 12, pp. 1–128, American Meteorological Society, Boston, MA, https://doi.org/10.1007/978-1-935704-34-8_1, 1972.
- Waelbroeck, C., Labeyrie, L., Michel, E., Duplessy, J. C., McManus, J. F., Lambeck, K., Balbon, E., and Labracherie, M.: Sea-level and deep water temperature changes derived from benthic foraminifera isotopic records, *Quaternary Science Reviews*, 21, 295–305, [https://doi.org/10.1016/S0277-3791\(01\)00101-9](https://doi.org/10.1016/S0277-3791(01)00101-9), 2002.
- 630 Weber, S. L. and Tuenter, E.: The impact of varying ice sheets and greenhouse gases on the intensity and timing of boreal summer monsoons, *Quaternary Science Reviews*, 30, 469–479, <https://doi.org/10.1016/j.quascirev.2010.12.009>, 2011.
- Ziegler, M., Tuenter, E., and Lourens, L. J.: The precession phase of the boreal summer monsoon as viewed from the eastern Mediterranean (ODP Site 968), *Quaternary Science Reviews*, 29, 1481–1490, <https://doi.org/10.1016/j.quascirev.2010.03.011>, 2010.
- 635